

Single-Nanowire Electrochemical Probe Detection for Internally Optimized Mechanism of Porous Graphene in Electrochemical Devices

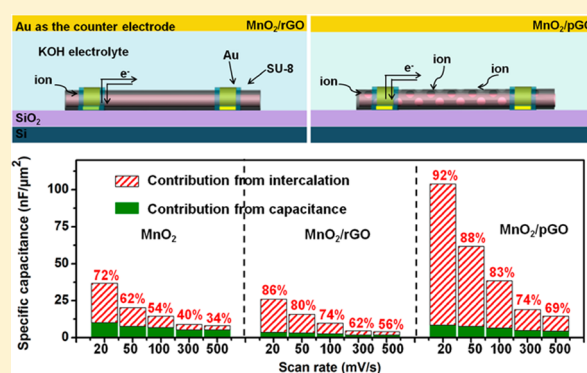
Ping Hu, Mengyu Yan, Xuanpeng Wang, Chunhua Han,* Liang He, Xiujuan Wei, Chaojiang Niu, Kangning Zhao, Xiaocong Tian, Qiulong Wei, Zijia Li, and Liqiang Mai*

State Key Laboratory of Advanced Technology for Materials Synthesis and Processing, Wuhan University of Technology, Wuhan 430070, China

S Supporting Information

ABSTRACT: Graphene has been widely used to enhance the performance of energy storage devices due to its high conductivity, large surface area, and excellent mechanical flexibility. However, it is still unclear how graphene influences the electrochemical performance and reaction mechanisms of electrode materials. The single-nanowire electrochemical probe is an effective tool to explore the intrinsic mechanisms of the electrochemical reactions in situ. Here, pure MnO₂ nanowires, reduced graphene oxide/MnO₂ wire-in-scroll nanowires, and porous graphene oxide/MnO₂ wire-in-scroll nanowires are employed to investigate the capacitance, ion diffusion coefficient, and charge storage mechanisms in single-nanowire electrochemical devices. The porous graphene oxide/MnO₂ wire-in-scroll nanowire delivers an areal capacitance of 104 nF/μm², which is 4.0 and 2.8 times as high as those of reduced graphene oxide/MnO₂ wire-in-scroll nanowire and MnO₂ nanowire, respectively, at a scan rate of 20 mV/s. It is demonstrated that the reduced graphene oxide wrapping around the MnO₂ nanowire greatly increases the electronic conductivity of the active materials, but decreases the ion diffusion coefficient because of the shielding effect of graphene. By creating pores in the graphene, the ion diffusion coefficient is recovered without degradation of the electron transport rate, which significantly improves the capacitance. Such single-nanowire electrochemical probes, which can detect electrochemical processes and behavior in situ, can also be fabricated with other active materials for energy storage and other applications in related fields.

KEYWORDS: Porous graphene oxide, ion transport, electron transport, nanowire, intercalation capacitance



It is a crucial scientific and engineering challenge for researchers to achieve high-efficiency and rechargeable energy storage devices.¹ Among main energy storage devices, batteries and supercapacitors, which show great potential for applications in electric vehicles, portable electronic devices, and uninterrupted power supplies,^{2–5} both rely on electrochemical processes, although separate electrochemical mechanisms determine their relative energy and power density.^{6–11} The electrochemical mechanisms of energy storage devices can be classified as either ion adsorption or redox reactions.^{12–16} Ion adsorption stores energy through electrostatic charge accumulation on the electrode/electrolyte interface of the materials, which is a non-Faradaic process.^{17–21} Redox reactions can be further classified into two types, namely, surface redox reactions and intercalation redox reactions.²² Surface redox reactions store energy through a Faradaic process where chemical redox reactions occur on the surface of an active material.^{23,24} Intercalation redox reaction charge storage occurs in the bulk through the rapid reversible intercalation of ions.^{12–14,25} For electrochemical storage materials, especially supercapacitor

materials, the overall electrochemical capacity can be greatly increased by enhancing the intercalation capacity.

Graphene is usually used as an additive in active materials to improve the electrochemical performance due to its high intrinsic electrical conductivity,^{26–30} large theoretical surface area,³¹ excellent mechanical flexibility,³² and favorable chemical stability.³³ Cui et al. used graphene to increase the electronic and ionic conductivities of MnO₂,³⁴ resulting in a substantial increase (20%) in the specific capacitance. However, Duan et al. and Han et al. reported that graphene decreased the accessible surface area and diffusion rate of ions.^{35,36} Hence, how graphene influences the electrochemical performance and reaction mechanisms of electrode materials is under dispute.

Single-nanowire electrochemical probes are effective tools to explore intrinsic electrochemical processes and behavior at a nanoscale level in situ. With the development of nanosized

Received: September 5, 2015

Revised: January 29, 2016

Published: February 16, 2016

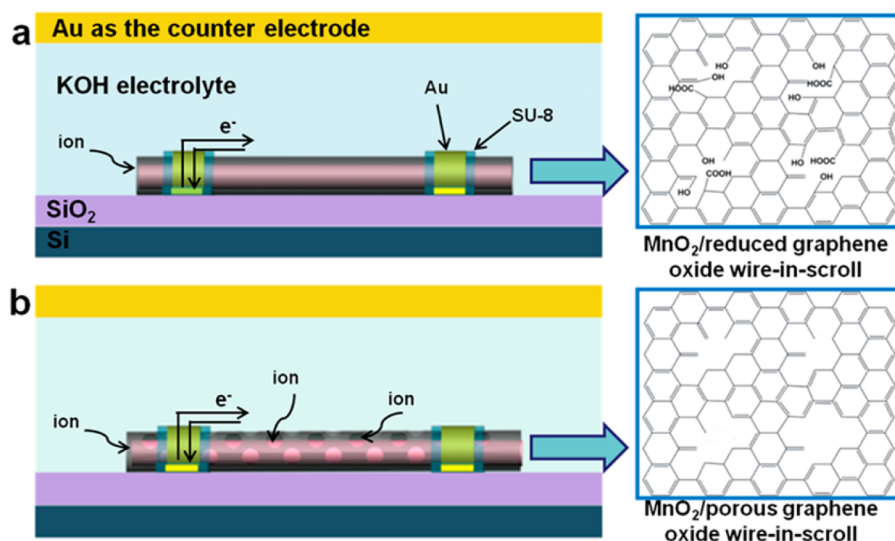


Figure 1. Schematic illustrations of single-nanowire electrochemical devices. (a) Schematic illustration of a MnO_2/rGO NW device and reduced graphene oxide. Ions transport only through the gap between the graphene and the MnO_2 NW. (b) Schematic illustration of a MnO_2/pGO NW device and porous graphene oxide. Ions transport through not only the gap between the graphene and the MnO_2 NW but also the pores in the graphene.

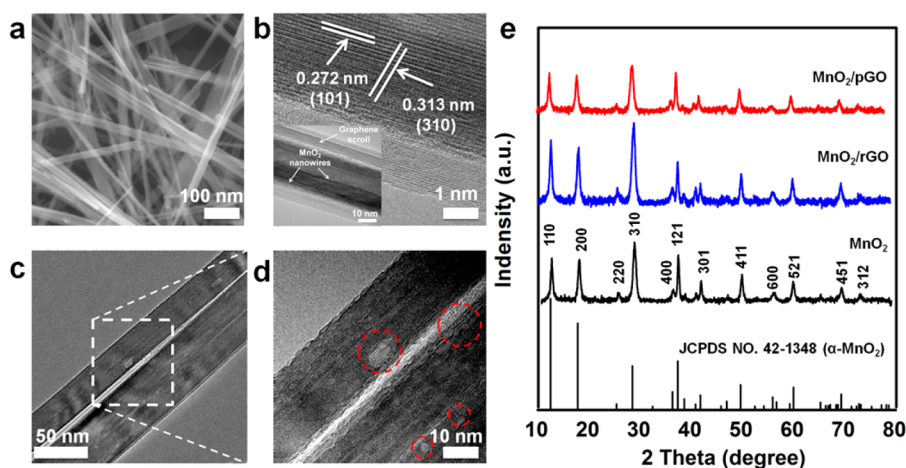


Figure 2. Structures of as-prepared samples, MnO_2 , MnO_2/rGO , and MnO_2/pGO NWs. (a) SEM image of MnO_2/pGO NWs. (b) TEM image of the edge of a MnO_2/rGO NW, showing that it includes two parts, MnO_2 NW (inside) and multilayer graphene (outer). (c) TEM image of a MnO_2/pGO NW. (d) HRTEM image of the edge of a MnO_2/pGO NW, showing pores in the material. (e) X-ray diffraction patterns of MnO_2 , MnO_2/rGO , and MnO_2/pGO NWs.

probes, single-nanowire electrochemical devices have been investigated and applied in field effect transistors,^{37,38} biosensors,^{39–41} batteries,^{42–44} and capacitors.²² Our group reported that a single-nanowire electrode device in situ detected an intrinsic factor for electrode capacity fading in Li ion-based energy storage devices.⁴² Ajayan et al. reported a single-nanowire capacitor fabricated with a $\text{Cu}-\text{Cu}_2\text{O}-\text{C}$ nanowire, which showed a high capacitance of $140 \mu\text{F}/\text{cm}^2$, exceeding previously reported values of metal–insulator–metal micro/nanocapacitors with capacitance densities ranging from 2.5 to $100 \mu\text{F}/\text{cm}^2$. The noise of this single nanowire capacitor was suppressed down to 2 fF in a wide frequency range (10^3 – 10^6 Hz).²² However, the capacitance of single-nanowire capacitors based on $\text{Cu}-\text{Cu}_2\text{O}-\text{C}$ nanowires is still far from satisfactory.

Herein, three configurations, pure MnO_2 nanowires (MnO_2 NWs), reduced graphene oxide/ MnO_2 wire-in-scroll nanowires (MnO_2/rGO NWs), and porous graphene oxide/ MnO_2 wire-

in-scroll nanowires (MnO_2/pGO NWs), are designed and employed to fabricate single-nanowire electrochemical devices. These single-nanowire electrochemical devices are measured to detect the electrochemical behavior of different structures and explore how graphene affects the active materials. Compared with that of MnO_2 NWs, the ion transport rate of the MnO_2/rGO NWs is largely limited by graphene because ions can only be transported through the gap between the graphene and the MnO_2 NWs. Though the electronic conductivity of MnO_2 is greatly improved for MnO_2/rGO , the MnO_2 is not completely immersed in the electrolyte to ensure full reaction (Figure 1a). The MnO_2/pGO NWs are produced by creating pores in the graphene of MnO_2/rGO (Figure 1b). In this way, ions are able to transport through not only the gap between the graphene and the MnO_2 NWs but also the pores in the graphene. Moreover, the pores in the graphene are sufficiently large to constitute a highly continuous network with open channels for ion transport. Meanwhile, the electronic conductivity of MnO_2

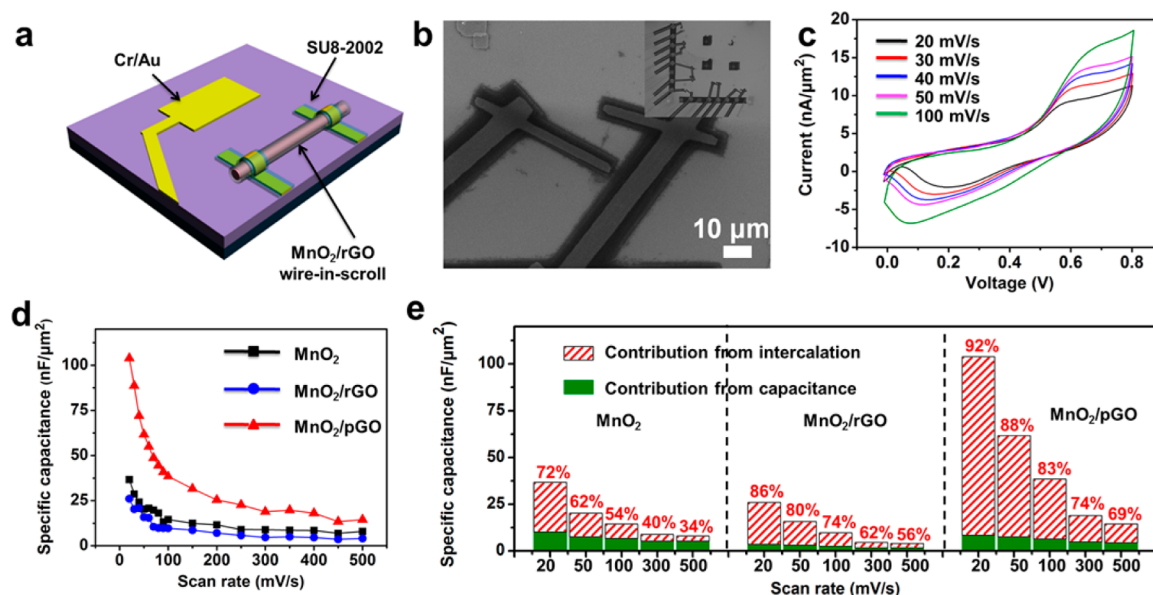


Figure 3. Schematic illustrations and electrochemical performances of single-nanowire electrochemical devices. (a) Schematic diagram of a single-nanowire electrochemical device. (b) Optical image of a single-nanowire electrochemical device. (c) The CV curves tested at scan rates of 20, 30, 40, 50, and 100 mV/s for the as-prepared MnO_2/pGO single-nanowire electrochemical device in 6 mol/L KOH. (d) The specific capacitance versus scan rates of as-prepared MnO_2 , MnO_2/rGO , and MnO_2/pGO single-nanowire electrochemical devices in 6 mol/L KOH. (e) Bar chart showing total capacitance in $\text{nF}/\mu\text{m}^2$ together with the percentage contribution from capacitance and intercalation as a function of different materials. The values are calculated results using CV curves recorded at scan rates of 20, 50, 100, 300, and 500 mV/s.

is significantly improved. The single-nanowire electrochemical device based on MnO_2/pGO delivers an areal capacitance of $104 \text{ nF}/\mu\text{m}^2$, which is 4.0 and 2.8 times as high as those of MnO_2/rGO and MnO_2 NWs, respectively, at a scan rate of 20 mV/s.

The construction processes of a nanowire template graphene scroll include the rapid growth and the self-scrolling of graphene ribbons (Figure S1 in the Supporting Information).⁴⁵ The morphologies of the samples with different hydrothermal times, including 3, 6, 12, and 18 h, are investigated (Figure S2). Scanning electron microscopy (SEM) shows a mixture of MnO_2 NWs and graphene when the reaction time is 3 h. With increased hydrothermal time, the graphene wraps around the MnO_2 nanowire to form the wire-in-scroll structure. These morphologies are in agreement with the construction process concepts (Figure S1). Furthermore, the crystal structures are characterized by X-ray diffraction (XRD) measurement. The diffraction peaks of the obtained MnO_2 and MnO_2/rGO are assigned to orthorhombic MnO_2 , which is in good agreement with JCPDS 72-1982 (Figure 2e). To examine further the morphologies and detailed structures of the samples, SEM and transmission electron microscopy (TEM) are employed. Low-magnification SEM shows that MnO_2/rGO NWs (Figure S3c) consist of two parts, graphene (outer) and MnO_2 NW (inside). The MnO_2/rGO NWs are 10–40 μm in length and 40–150 nm in diameter, much longer and wider than the pure MnO_2 NWs (Figure S3a,b). The above phenomena can be attributed to the confinement effect of graphene during the formation processes of wire-in-scroll structures.⁴⁶ TEM of a MnO_2/rGO NW (Figure 2b) shows that the MnO_2 NW is scrolled inside the graphene. The lattice spacings of 0.272 and 0.313 nm match well with the separation distances between (101) and (310) planes, respectively. The MnO_2 NWs shows a preferred {310} growth orientation. At the edge of a MnO_2 NW, 20 layers of graphene are observed with a lattice spacing of 0.734 nm.

The MnO_2/pGO NWs are prepared by reducing MnO_2/rGO NWs with 10 mmol/L hydrazine hydrates for 3 h. The main XRD peaks of MnO_2/pGO exhibit no substantial changes from those of MnO_2 and MnO_2/rGO , demonstrating that the phases remain the same during the hydrazine hydrate treatment. With increasing hydrating time from 6 to 12 and 24 h, the XRD patterns change substantially; the peak intensities of Mn_3O_4 increase, and the peak intensities of MnO_2 decrease. With the reduction time of 24 h, the crystal structure of the material transfers to orthorhombic Mn_3O_4 (JCPDS 16-0154) (Figure S5). The morphology of the samples after hydrazine hydrate treatment for 6, 12, and 24 h also change greatly. Increasing amounts of graphene separates from the wire-in-scroll structure with increasing hydrazine hydrate treatment time (Figures S3d–f and S4). Thus, a hydrazine hydrate treatment time of 3 h is chosen as the most suitable time for producing MnO_2/pGO . An SEM image of MnO_2/pGO NWs is shown in Figure 2a. The MnO_2/pGO NWs are also composed of two parts, graphene (outer) and MnO_2 nanowire (inside), similar to the MnO_2/rGO NWs. TEM of MnO_2/pGO NWs (Figure 2c,d) demonstrates that MnO_2/pGO NWs exhibit hexagonal pores of different sizes; the maximum pore diameter reaches 5 nm. This finding is attributed to oxygen-containing functional groups in the graphene of MnO_2/rGO NWs, which are removed by hydrazine hydrate.

The Raman spectra of MnO_2 , MnO_2/rGO , MnO_2/pGO show no obvious differences; this is due to the low graphene contents (3.38 wt %) (Figure S6). D and G bands are not discernible in the MnO_2/rGO and MnO_2/pGO spectra (Figure S7). The X-ray photoelectron spectra of these materials shown in Figure S8 are used to investigate whether oxygen vacancies exist in MnO_2 . The O 1s core level spectra are used to confirm the presence of oxygen vacancies in MnO_2 . The spectra are fit well with two components, the Mn–O–Mn bond (529.7 eV)

of tetravalent oxide and the Mn–OH bond (531.43 eV) of hydrated trivalent oxide.^{47,48} Quantitative analysis shows that the oxygen vacancies exist in MnO₂, which results from the existence of Mn³⁺ in MnO₂ (13.84%).

The fabrication processes of single-nanowire electrochemical devices are shown in Figure S9. Single-nanowire devices, where a single nanowire serves as the working electrode, one flake of Au serves as the counter electrode, and 6 mol/L KOH serves as the electrolyte, are assembled to detect the electrochemical performances of these three different nanowire structures (Figure 3a). The structure of single-nanowire electrochemical device test system under SEM is shown in Figure 3b. The electrochemical performances of these single-nanowire electrochemical devices are tested to investigate how graphene affects the performance of active materials. The cyclic voltammetry (CV) curves of MnO₂ NWs (Figure S10), MnO₂/rGO NWs (Figure S10), and MnO₂/pGO NWs (Figure 3c) at scan rates from 20 to 100 mV/s are given. The specific capacitances of electrochemical devices can be calculated based on the following equation⁴⁹

$$C = \frac{\int Idv}{2SA\Delta V} \quad (1)$$

where I represents the working current, S represents the scanning rates, A represents the electrode area of the nanowires, and ΔV represents the voltage range.

The specific capacitances calculated from the CV curves are illustrated in Figure 3d. The MnO₂/pGO NWs exhibits an ultrahigh surface capacitance of 104 nF/ μm^2 at a scan rate of 20 mV/s. In contrast, the specific capacitances of the MnO₂ NWs and MnO₂/rGO NWs are merely 37 and 26 nF/ μm^2 , respectively, at a scan rate of 20 mV/s. With the scan rate increasing up to 500 mV/s, the MnO₂/pGO NWs still displays a high specific capacitance of 15 nF/ μm^2 , while those of the MnO₂ and MnO₂/rGO NWs are only 8 and 4 nF/ μm^2 , respectively.

I – V curves and EIS plots are further collected to investigate the reason of the MnO₂/pGO NWs shows excellent areal specific capacitance. The transport properties of different single nanowires are determined by testing the I – V curves (Figure S11). The conductivity of the MnO₂/pGO NWs reaches a high value of 328 S/m, which is 1.4 and 3.8 times higher than those of the MnO₂/rGO and MnO₂ NWs, respectively. The diffusion coefficient value (D) of ions can be calculated using eq 2

$$D = \frac{R^2 T^2}{2A^2 n^4 F^4 C^2 \sigma^2} \quad (2)$$

where R represents the gas constant, T represents the absolute temperature, A represents the area of the electrode surface, n represents the number of electrons transferred in the half-reaction for the redox couple, F represents Faraday's constant, C represents the molar concentration of ions, and σ is associated with Z_{re} , which can be determined by eq 3⁵⁰

$$Z_{\text{re}} = R_D + R_L + \sigma \omega^{-1/2} \quad (3)$$

According to the linear fit, the slope of the real part of the complex impedance versus $\omega^{-1/2}$ at the potential of 0.3 V (vs HgCl/Hg) for MnO₂, MnO₂/rGO, and MnO₂/pGO NWs is 4.08×10^6 , 4.39×10^7 and 7.06×10^6 , respectively. (The response of AC impedance changes noisily when the frequency is below 10^3 Hz. Only impedance data in the frequency range of 10^3 – 10^6 Hz is stable in the single-nanowire system.²²) The ion

diffusion coefficients at room temperature of the MnO₂, MnO₂/rGO, and MnO₂/pGO NWs are calculated to be 5.55×10^{-8} , 5.21×10^{-9} , and 2.31×10^{-8} cm² s⁻¹, respectively (Figure S12). Reduced graphene oxide wrapping around a MnO₂ nanowire leads to a decrease of the ion diffusion coefficient resulting from the shielding effect of graphene. By creating pores in the graphene, the ion diffusion coefficient can be recovered.

The above results indicate that when reduced graphene oxide wraps around a MnO₂ (MnO₂/rGO) nanowire, the electronic conductivity of MnO₂ is greatly improved. However, the ion diffusion coefficient is limited by the graphene. Then, when pores are created in the rGO of MnO₂/pGO, the ion transport properties of the active materials are enhanced without degradation of the electron transfer rate. More active materials can be utilized to contribute to the capacitance, leading to significant improvements.

Optimization of these mechanisms between graphene and active materials are further investigated. The total stored charge shown in Figure 3d is separated into two components: the contributions from surface capacitance and diffusion-controlled ion insertion capacitance. Therefore, the current response (i) at a fixed potential (V) can be described as the sum of two contributions arising from the capacitive and intercalation capacity, as discussed below^{13,51–53}

$$i(V) = k_1 \mu + k_2 \mu^{0.5} \quad (4)$$

or

$$i(V)/\mu^{0.5} = k_1 \mu^{0.5} + k_2 \quad (5)$$

where μ represents the sweep rate, and $k_1 \mu$ and $k_2 \mu^{0.5}$ correspond to the current contributions from the capacitive (surface pseudocapacitance and double-layer capacitance) and insertion processes (insertion pseudocapacitance), respectively. By determining k_1 and k_2 , it is possible to distinguish the fractions of current arising from capacitive and insertion processes at specific potentials (Figure S13).

This mode is a general method to separate the contribution proportions of surface and intercalation capacitance, which can also be used in the single-nanowire device system. This analysis is used to determine the fraction of the total stored charge from capacitive processes as a function of scan rate. The overall charge proportions of capacitive and insertion processes are shown in Figure 3e. As the scan rate increases, the capacitance of the NW device decreases. This behavior is attributed to the fact that the higher scan rate prevents ion access into the MnO₂ nanowire. At a higher scan rate, the movement of ions is limited, which is due to their slow diffusion. Thus, only the outer surface of the electrode material can be utilized for charge storage.⁵⁴ For all three of these single-nanowire electrochemical devices, capacitance is negatively correlated with scan rate. The degradation of capacitance is mainly due to the decrease of intercalation capacitance at a relatively high scan rate with little influence from the surface capacitance. The MnO₂/pGO NWs exhibits a specific capacitance of 104 nF/ μm^2 out of which 95 nF/ μm^2 (20 mV/s) corresponds to ion intercalation into the MnO₂ NWs and 9 nF/ μm^2 corresponds to the surface reaction. The intercalation capacitance proportions of the MnO₂/pGO NWs are 92%, 83%, 69% (MnO₂/rGO NW, 86%, 74%, 56%; MnO₂ NW, 72%, 54%, 34%) at the scan rates of 20, 100, and 500 mV/s, respectively. In this single-nanowire electrochemical device system, MnO₂ can sufficiently react with ions in KOH

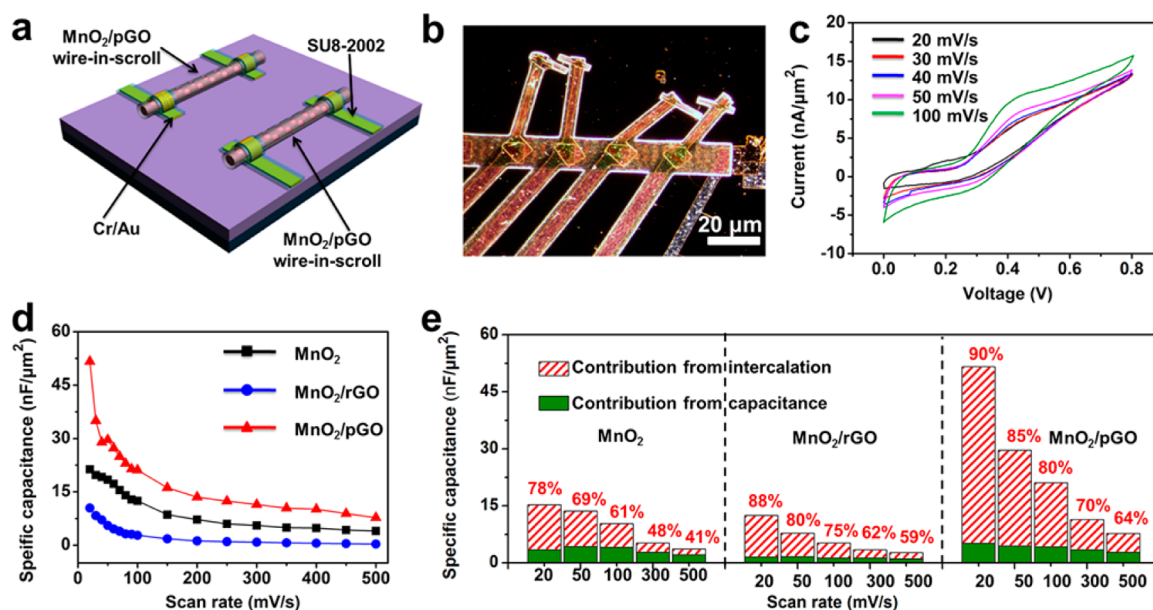


Figure 4. Schematic illustrations and electrochemical performances of symmetric single-nanowire electrochemical devices. (a) Schematic diagram of a symmetric single-nanowire electrochemical device. (b) Optical image of a symmetric single-nanowire electrochemical device. (c) The CV curves at scan rates of 20, 30, 40, 50, and 100 mV/s for the as-prepared MnO₂/pGO symmetric single-nanowire electrochemical devices in 6 mol/L KOH. (d) The specific capacitance versus scan rates of as-prepared symmetric single-nanowire electrochemical devices in 6 mol/L KOH. (e) Bar chart showing total capacitance in nF/μm² together with percent contribution from capacitance and intercalation as a function of different materials. The values are calculated using CV curves recorded at scan rates of 20, 50, 100, 300, and 500 mV/s.

electrolyte without any environmental interference. Thus, ions can access the materials more easily, which results in higher contributions from intercalation in the NW devices. At the same scan rate, the surface capacitance of the MnO₂/rGO NWs is the lowest among these three devices due to the limited ion transfer speed. Ions only transport through the gap between the graphene and the MnO₂ NW. The ion diffusion coefficient of MnO₂/rGO is approximately an order of magnitude lower than that of MnO₂ (Figure S12). Though the electronic conductivity is greatly improved, the surface of MnO₂ cannot be completely immersed in electrolyte, which leads to a decrease of surface capacitance. Meanwhile, the intercalation capacitances of MnO₂, MnO₂/rGO, and MnO₂/pGO remain unchanged. The total capacitance and the percentage of intercalation capacitance of the MnO₂/pGO NWs are higher than those of MnO₂ and MnO₂/rGO NWs at each scan rate, which can be attributed to pores in the graphene allowing the transportation of ions. The pores in the graphene provide more accessible surface areas for ions, efficient electron/ion transport pathways, and ion transport that is unlimited by graphene. Meanwhile, the electronic conductivity of MnO₂ shows no degradation. The above reasons support the increase in the intercalation capacity of MnO₂/pGO compared with those of MnO₂ and MnO₂/rGO.

Symmetric single-nanowire electrochemical devices are fabricated with two nanowires as working and counter electrodes, respectively (Figure 4a,b). The electrochemical performances of the symmetric single-nanowire electrochemical devices are also evaluated by cyclic voltammetry tests at different scan rates. For comparison, CV tests of MnO₂/pGO (Figure 4c), MnO₂ (Figure S14), and MnO₂/rGO (Figure S14) symmetric single-nanowire electrochemical device at the scan rates of 20–100 mV/s are conducted. To demonstrate the faradaic current contributions from background processes on the surface of the contact electrodes, the CV curves for MnO₂/pGO symmetric single-nanowire electrochemical devices and

background processes are provided (Figure S15). The quantity of electric charge of background processes on the surface of the contact electrodes with an SU-8 passivation layer is 1.09×10^{-11} C, which is much lower than that of the MnO₂/pGO (2.57×10^{-10} C) at a scan rate of 100 mV/s. Thus, the faradaic current of the background processes on the surface of the contact electrodes with an SU-8 passivation layer can be considered negligible (Figure S15). The specific capacitance of the MnO₂/rGO NWs is calculated to be smaller than that of the MnO₂ NWs at each scan rate. The specific capacitance of the MnO₂/pGO NWs is much higher than that of the MnO₂ NWs at various scan rates (Figure 4d). MnO₂/pGO, MnO₂/rGO, and MnO₂ NWs display high capacitances of 52, 13, and 15 nF/μm², respectively, at a scan rate of 20 mV/s. At a high scan rate of 500 mV/s, the MnO₂/pGO NWs maintain a capacitance of 8 nF/μm², which is 2.9 and 2.1 times higher than those of the MnO₂/rGO and MnO₂ NWs. The performance tendencies of these three devices are consistent with those of the single-nanowire devices. Moreover, we also investigate the different contributions in those three configurations; similar tendencies are also observed, except for a slight decrease in capacity. The performance tendency (Figure 4e) of the fraction of the total stored charge from capacitive processes as a function of scan rate is similar in the symmetric single-nanowire electrochemical devices and the asymmetric single-nanowire electrochemical devices (Figure 3e).

In summary, a single-nanowire electrochemical probe is employed to detect how graphene influences the performance and electrochemical reaction mechanisms of electrode materials at the nanoscale level in which MnO₂, MnO₂/rGO, and MnO₂/pGO NWs are used. The single-nanowire electrochemical device based on MnO₂/pGO NWs exhibits a reversible, high capacitance of 104 nF/μm², which is 4.0 and 2.8 times as high as those of the MnO₂/rGO and MnO₂ NWs, respectively, at a scan rate of 20 mV/s. It demonstrates that porous graphene

increases the capacitance of single MnO₂ nanowires, mainly by increasing MnO₂ NWs intercalation capacitance. The pores in the graphene provide channels for ion diffusion without degrading the rate of electron transport. The above results are further verified by symmetric single-nanowire electrochemical devices. The single-nanowire electrochemical probe for in situ detection of intrinsic electrochemical processes and behavior shows potential for applications in energy storage and related fields.

■ ASSOCIATED CONTENT

Supporting Information

The Supporting Information is available free of charge on the ACS Publications website at DOI: 10.1021/acs.nanolett.5b03576.

Additional information, the experimental section, and figures are included. (PDF)

■ AUTHOR INFORMATION

Corresponding Authors

*E-mail: (C.H.) hch5927@whut.edu.cn.

*E-mail: (L.M.) mlq518@whut.edu.cn.

Author Contributions

P.H. and M.Y. contributed equally to this work.

L.Q.M., C.H.H., P.H., and M.Y.Y. designed the experiments. P.H., M.Y.Y., L.H., X.P.W., and Z.J.L. performed the experiments. P.H., M.Y.Y., X.J.W., C.J.N., K.N.Z., X.C.T., and Q.L.W. discussed the interpretation of results and cowrote the paper. All authors have given approval of the final version of the manuscript.

Notes

The authors declare no competing financial interest.

■ ACKNOWLEDGMENTS

This work was supported by the National Basic Research Program of China (2013CB934103, 2012CB933003), the International Science and Technology Cooperation Program of China (2013DFA50840), the National Natural Science Foundation of China (51521001, 51272197), The National Natural Science Fund for Distinguished Young Scholars (51425204), The Hubei Province Natural Science Fund for Distinguished Young Scholars (2014CFA035), and the Fundamental Research Funds for the Central Universities (WUT: 152401004, 2014-YB-001, and 2014-YB-002). The authors thank Professor C. M. Lieber of Harvard University and Professor D. Y. Zhao of Fudan University for their strong support and stimulating discussion.

■ REFERENCES

- (1) Jiang, J.; Li, Y. Y.; Liu, J. P.; Huang, X. T.; Yuan, C. Z.; Lou, X. W. *Adv. Mater.* **2012**, *24*, 5166–5180.
- (2) Simon, P.; Gogotsi, Y.; Dunn, B. *Science* **2014**, *343*, 1210–1211.
- (3) Kim, D.; Shin, G.; Kang, Y. J.; Kim, W.; Ha, J. S. *ACS Nano* **2013**, *7*, 7975–7982.
- (4) Niu, C. J.; Meng, J. S.; Wang, X. P.; Han, C. H.; Yan, M. Y.; Zhao, K. N.; Xu, X. M.; Ren, W. H.; Zhao, Y. L.; Xu, L.; Zhang, Q. J.; Zhao, D. Y.; Mai, L. Q. *Nat. Commun.* **2015**, *6*, 7402.
- (5) Hall, P. J.; Mirzaei, M.; Fletcher, S. I.; Sillars, F. B.; Rennie, A. J.; Shitta-Bey, G. O.; Wilson, G.; Cruden, A.; Carter, R. *Energy Environ. Sci.* **2010**, *3*, 1238–1251.
- (6) Gowda, S. R.; Leela, M. R. A.; Zhan, X.; Ajayan, P. M. *Nano Lett.* **2011**, *11*, 3329–3333.

- (7) Zhai, Y.; Dou, Y.; Zhao, D.; Fulvio, P. F.; Mayes, R. T.; Dai, S. *Adv. Mater.* **2011**, *23*, 4828–4850.
- (8) Wang, X. P.; Niu, C. J.; Meng, J. S.; Hu, P.; Xu, X. M.; Wei, X. J.; Zhou, L.; Zhao, K. N.; Luo, W.; Yan, M. Y.; Mai, L. Q. *Adv. Energy Mater.* **2015**, *5*, 1500716.
- (9) Arico, A. S.; Bruce, P.; Scrosati, B.; Tarascon, J. M.; van Schalkwijk, W. *Nat. Mater.* **2005**, *4*, 366–377.
- (10) Peng, L.; Peng, X.; Liu, B. R.; Wu, C. Z.; Xie, Y.; Yu, G. H. *Nano Lett.* **2013**, *13*, 2151–2157.
- (11) Augustyn, V.; Come, J.; Lowe, M. A.; Kim, J. W.; Taberna, P. L.; Tolbert, S. H.; Abruña, H. D.; Simon, P.; Dunn, B. *Nat. Mater.* **2013**, *12*, 518–522.
- (12) Mefford, J. T.; Hardin, W. G.; Dai, S.; Johnston, K. P.; Stevenson, K. J. *Nat. Mater.* **2014**, *13*, 726.
- (13) Brezesinski, T.; Wang, J.; Tolbert, S. H.; Dunn, B. *Nat. Mater.* **2010**, *9*, 146–151.
- (14) Lukatskaya, M. R.; Mashtalir, O.; Ren, C. E.; Dall'Agnese, Y.; Rozier, P.; Taberna, P. L.; Naguib, M.; Simon, P.; Barsoum, M. W.; Gogotsi, Y. *Science* **2013**, *341*, 1502–1505.
- (15) Simon, P.; Gogotsi, Y. *Nat. Mater.* **2008**, *7*, 845–854.
- (16) Merlet, C.; Rotenberg, B.; Madden, P. A.; Taberna, P. L.; Simon, P.; Gogotsi, Y.; Salanne, M. *Nat. Mater.* **2012**, *11*, 306–310.
- (17) Kim, J. W.; Augustyn, V.; Dunn, B. *Adv. Energy Mater.* **2012**, *2*, 141–148.
- (18) Conway, B. E. *Electrochemical Supercapacitors: Scientific Fundamentals and Technological Applications*; Kluwer Academic/Plenum: New York, 1999.
- (19) Lang, X. Y.; Hirata, A.; Fujita, T.; Chen, M. W. *Nat. Nanotechnol.* **2011**, *6*, 232–236.
- (20) Frackowiak, E.; Beguin, F. *Carbon* **2001**, *39*, 937–950.
- (21) Augustyn, V.; Simon, P.; Dunn, B. *Energy Environ. Sci.* **2014**, *7*, 1597–1614.
- (22) Liu, Z.; Zhan, Y.; Shi, G.; Moldovan, S.; Gharbi, M.; Song, L.; Ma, L. L.; Gao, W.; Huang, J. Q.; Vajtai, R.; Banhart, F.; Sharma, P.; Lou, J.; Ajayan, P. M. *Nat. Commun.* **2012**, *3*, 879.
- (23) Sawangphruk, M.; Srimuk, P.; Chiochan, P.; Krittayathananon, A.; Luanwuthi, S.; Limtrakul, J. *Carbon* **2013**, *60*, 109–116.
- (24) Xie, J. F.; Sun, X.; Zhang, N.; Xu, K.; Zhou, M.; Xie, Y. *Nano Energy* **2013**, *2*, 65–74.
- (25) Zheng, J. P.; Jow, T. R. *Electrochem. Soc.* **1995**, *142*, 6–8.
- (26) El-Kady, M. F.; Strong, V.; Dubin, S.; Kaner, R. B. *Science* **2012**, *335*, 1326–1330.
- (27) Liu, C. G.; Yu, Z. N.; Neff, D.; Zhamu, A.; Jang, B. Z. *Nano Lett.* **2010**, *10*, 4863–4870.
- (28) Xu, Y. X.; Lin, Z. Y.; Huang, X. Q.; Wang, Y.; Huang, Y.; Duan, X. F. *Adv. Mater.* **2013**, *25*, 5779–5784.
- (29) Sun, Y. Q.; Wu, Q.; Shi, G. Q. *Energy Environ. Sci.* **2011**, *4*, 1113–1132.
- (30) Huang, Y.; Liang, J. J.; Chen, Y. S. *Small* **2012**, *8*, 1805–1834.
- (31) Choi, B. G.; Yang, M.; Hong, W. H.; Choi, J. W.; Huh, Y. S. *ACS Nano* **2012**, *6*, 4020–4028.
- (32) Zhu, Y.; Murali, S.; Cai, W.; Li, X.; Suk, J. W.; Potts, J. R.; Ruoff, R. S. *Adv. Mater.* **2010**, *22*, 3906–3924.
- (33) Zhu, Y.; Murali, S.; Stoller, M. D.; Ganesh, K. J.; Cai, W.; Ferreira, P. J.; Pirkle, A.; Wallace, R. M.; Cychosz, K. A.; Thommes, M.; Su, D.; Stach, E. A.; Ruoff, R. S. *Science* **2011**, *332*, 1537–1541.
- (34) Yu, G. H.; Hu, L. B.; Liu, N.; Wang, H. L.; Vosgueritchian, M.; Yang, Y.; Cui, Y.; Bao, Z. N. *Nano Lett.* **2011**, *11*, 4438–4442.
- (35) Xu, Y. X.; Lin, Z. Y.; Zhong, X.; Huang, X. Q.; Weiss, N. O.; Huang, Y.; Duan, X. F. *Nat. Commun.* **2014**, *5*, 4554.
- (36) Zhou, D.; Cui, Y.; Xiao, P. W.; Jiang, M. Y.; Han, B. H. *Nat. Commun.* **2014**, *5*, 4716.
- (37) Duan, X. J.; Gao, R. X.; Xie, P.; Cohen-Karni, Y.; Qing, Q.; Choe, H. S.; Tian, B. Z.; Jiang, X. C.; Lieber, C. M. *Nat. Nanotechnol.* **2011**, *7*, 174–179.
- (38) Xu, L.; Jiang, Z.; Qing, Q.; Mai, L. Q.; Zhang, Q. J.; Lieber, C. M. *Nano Lett.* **2013**, *13*, 746–751.

- (39) Sarkar, D.; Liu, W.; Xie, X.; Anselmo, A. C.; Mitragotri, S.; Banerjee, K. *ACS Nano* **2014**, *8*, 3992–4003.
- (40) Cai, B.; Wang, S.; Huang, L.; Ning, Y.; Zhang, Z.; Zhang, G. J. *ACS Nano* **2014**, *8*, 2632–2638.
- (41) Duan, X. X.; Li, Y.; Rajan, N. K.; Routenberg, D. A.; Modis, Y.; Reed, M. A. *Nat. Nanotechnol.* **2012**, *7*, 401–407.
- (42) Mai, L. Q.; Dong, Y. J.; Xu, L.; Han, C. H. *Nano Lett.* **2010**, *10*, 4273–4278.
- (43) Tian, X. C.; Xu, X.; He, L.; Wei, Q. L.; Yan, M. Y.; Xu, L.; Zhao, Y. L.; Yang, Y.; Mai, L. Q. *J. Power Sources* **2014**, *255*, 235–241.
- (44) Xu, X.; Yan, M. Y.; Tian, X. C.; Yang, C. C.; Shi, M. Z.; Wei, Q. L.; Xu, X.; Mai, L. Q. *Nano Lett.* **2015**, *15*, 3879–3884.
- (45) Yan, M. Y.; Wang, F. C.; Han, C. H.; Ma, X. Y.; Xu, X.; An, Q. Y.; Xu, L.; Niu, C. J.; Zhao, Y. L.; Tian, X. C.; Hu, P.; Wu, H. A.; Mai, L. Q. *J. Am. Chem. Soc.* **2013**, *135*, 18176–18182.
- (46) Balog, R.; Jørgensen, B.; Nilsson, L.; Andersen, M.; Rienks, E.; Bianchi, M.; Mattia, F.; Lægsgaard, E.; Baraldi, A.; Lizzit, S.; Slijivancanin, Z.; Besenbacher, F.; Hammer, B.; Pedersen, T. G.; Hofmann, P.; Hornekær, L. *Nat. Mater.* **2010**, *9*, 315–319.
- (47) Toupin, M.; Brousse, T.; Bélanger, D. *Chem. Mater.* **2004**, *16*, 3184–3190.
- (48) Banerjee, D.; Nesbitt, H. W. *Geochim. Cosmochim. Acta* **2001**, *65*, 1703–1714.
- (49) Mai, L. Q.; Minhas-Khan, A.; Tian, X. C.; Hercule, K. M.; Zhao, Y. L.; Lin, X.; Xu, X. *Nat. Commun.* **2013**, *4*, 2923.
- (50) Shi, Y.; Wang, J. Z.; Chou, S. L.; Wexler, D.; Li, H. J.; Ozawa, K.; Liu, H. K.; Wu, Y. P. *Nano Lett.* **2013**, *13*, 4715–4720.
- (51) Sathiya, M.; Prakash, A. S.; Ramesha, K.; Tarascon, J. M.; Shukla, A. K. *J. Am. Chem. Soc.* **2011**, *133*, 16291–16299.
- (52) Bard, A. J.; Faulkner, L. R. *Electrochemical Methods: Fundamentals and Applications*; Wiley: New York, 1980.
- (53) Lindström, H.; Södergren, S.; Solbrand, A.; Rensmo, H.; Hjelm, J.; Hagfeldt, A.; Lindquist, S. E. *J. Phys. Chem. B* **1997**, *101*, 7717–7722.
- (54) Rakhi, R. B.; Chen, W.; Cha, D. K.; Alshareef, H. N. *Nano Lett.* **2012**, *12*, 2559–2567.